Supporting Information for "Nonlinear dynamics of the near-shore boundary layer of a large lake (Lake Geneva)"

Andrea A. Cimatoribus[1], U. Lemmin[1], D. Bouffard[2], and D. A. Barry[1]

Contents of this file

Introduction

This supporting information presents:

• Details on the model configuration (Text S1).

• Further validation of the model results not presented in the main article (Text S2, Figures S1 and S2).

• Figure S3, comparing velocity time series in the model and observations at some locations.

• Figure S4, showing the temperature variance spectra.

Text S1. Model configuration

The model used the MITgcm code [*Marshall et al.*, 1997] to solve the three-dimensional Navier-Stokes equations under the incompressible, Boussinesq and hydrostatic approximations, with a finite volume approach. The model configuration was derived from *Hill et al.* [2012], who used a nonlinear advection scheme [*Prather*, 1986] for temperature to limit numerical diffusion. The nonlinear equation of state of *McDougall et al.* [2003] was applied, with a constant salinity of 0.05 p.s.u. The Coriolis force was included, assuming a constant rotation rate over the domain (f-plane), with Coriolis frequency $f = 1.05 \times 10^{-4}\,\mathrm{s}^{-1}$.

In the Low Resolution (LR) simulation, equations were solved on an orthogonal curvilinear grid having variable horizontal resolution ranging from $173\,\mathrm{m}$ to $260\,\mathrm{m}$ (square root of cell area). Care was taken to ensure that the aspect ratio of the cells was close to one, within 10%. The model used z-coordinates with 35 vertical levels ranging in thickness from $0.5\,\mathrm{m}$ at the top to $37\,\mathrm{m}$ at the bottom. In the High Resolution (HR) simulations, equations were solved on a square grid with a horizontal resolution of $113\,\mathrm{m}$. The model had 50 vertical levels ranging in thickness from $0.3\,\mathrm{m}$ at the top to $12\,\mathrm{m}$ at the bottom. Model bathymetry in both configurations was interpolated from the high resolution survey conducted by the Canton Vaud (Switzerland) in 2014 (Figure 1). "Shaved cells" were used, adapting the bottom grid cell thickness to the locally measured bathymetry [*Adcroft et al.*, 1997]. A semi-implicit free surface was included.

Due to the limited amount of velocity observations available, a systematic calibration of the model was not possible. The values of viscosity were instead chosen by manual tuning, as commonly done for large-scale flow simulations, based on repeated simulations using different configurations spanning the period from February to April 2014.

Bottom friction was computed as the frictional stress $\tau_B = C_D \rho \|\mathbf{u}\| \mathbf{u}$, with ρ the water density, $\mathbf{u}$ the velocity vector and $\|\mathbf{u}\|$ its magnitude. The non-dimensional coefficient was set to $C_D = 0.003$ (LR) or $C_D = 0.0025$ (HR) based on the values measured by *Bouffard and Lemmin* [2013] at the confluence between the Petit and Grand Lac ($C_D = 0.0025$). Lateral boundary conditions are no-slip in the HR configuration. Dissipation at the side boundary is always weaker than bottom friction and, in the LR model, free-slip side boundary conditions are used.

As noted by *Dorostkar et al.* [2010], bulk viscosity is of secondary importance in an enclosed domain, and results are insensitive to this parameter below a threshold, whereas the flow is increasingly smooth above it. Here, the model was configured to obtain numerical stability with minimum viscosity. In the LR configuration, biharmonic viscosity (proportional to $\nabla^4 \mathbf{u}$) was used; the biharmonic viscosity coefficient was given by $1/32\,\ell^4\,A_4/\Delta t$, with ℓ the local grid length scale, Δt the time step and A_4 a non-dimensional coefficient set to 0.05. Biharmonic viscosity is a common choice in ocean modeling, enabling the inclusion of motions over a broader range of scales on a given grid, still guaranteeing numerical stability [*Griffies and Hallberg*, 2000]. "Standard" (Laplacian) molecular background viscosity was included in the horizontal and vertical directions. In the HR version of the model, Smagorinsky Laplacian horizontal viscosity with a coefficient of 0.3 was used [*Griffies and Hallberg*, 2000], given the finer grid. Biharmonic viscosity with a coefficient $A_4 = 0.01$ was included for numerical stability. Results from the LR and HR models are broadly consistent, with major differences only near the shore.

Vertical mixing was modeled with the simple one-equation turbulence closure of *Gaspar et al.* [1990]. After extensive testing in a single column configuration, the values of the parameters given in *Gaspar et al.* [1990] were used, in combination with an increased diffusivity under unstable stratification ($0.02\,\mathrm{m}^2\,\mathrm{s}^{-1}$) to improve the modeling of convection. Vertical stratification was more sensitive to changes in background diffusivity. Based on the results from the single column model, this was set to the molecular value (horizontal diffusivity was set to the same molecular value).

Time integration was performed with a constant time step of $20\,\mathrm{s}$ for the LR case, $6\,\mathrm{s}$ for the HR case. The LR simulations were run on 5 CPUs (clock frequency $3.3\,\mathrm{GHz}$) producing approximately $100\,\mathrm{s}$ of results in $1\,\mathrm{s}$. HR simulations were run on 196 CPUs (clock frequency $2.6\,\mathrm{GHz}$) obtaining a similar speed.

Surface forcing was derived from the atmospheric fields of the MeteoSwiss numerical weather prediction model COSMO (hourly data, horizontal resolution of $2\,\mathrm{km}$ reduced to $1\,\mathrm{km}$ after 23 August 2016), using the bulk formulas of *Large and Yeager* [2004]. These were developed for the ocean case, but give good results for Lake Geneva. The wind drag coefficients described in *Wüest and Lorke* [2003] were tested, but did not lead to any clear improvement of the results. The model was forced by surface momentum flux (wind stress), by surface heat flux (evaporation, long-wave radiation, conduction) and by shortwave radiative heating, with the latter being the only term distributed at different

[1]Ecological Engineering Laboratory (ECOL), Institute of Environmental Engineering (IIE), School of Architecture, Civil and Environmental Engineering (ENAC), École Polytechnique Fédérale de Lausanne (EPFL), 1015 Lausanne, Switzerland

[2]Aquatic Physics group, Department of Surface Waters Research and Management, Swiss Federal Institute of Aquatic Science and Technology (EAWAG), 6047 Kastanienbaum, Switzerland and Physics of Aquatic Systems Laboratory (APHYS), Institute of Environmental Engineering, School of Architecture, Civil and Environmental Engineering, École Polytechnique Fédérale de Lausanne (EPFL), 1015 Lausanne, Switzerland

depths due to the absorption of light by the water [water type 1B in *Paulson and Simpson*, 1977]. Concerning the forcing, we note that the COSMO model, from which the atmospheric forcing is extracted, lacks a consistent daily wind cycle, probably due to an underestimation of the temperature contrast between land and water that drives these winds [*Lemmin and D'Adamo*, 1997; *MeteoSwiss*, 2017].

The discharge of the Rhône river was included in the model, entering the domain at the eastern end of the lake. The same volume flux exited at the western end of the basin (see Figure 1). Volume flow and temperature measurements of the Rhône river discharge every 10 min were obtained from the Federal Office for the Environment (OFEN), Switzerland, on 7 March 2017. The impact of river discharge on the general circulation is minor.

Text S2. Model Validation

Vertical temperature profiles

The collected vertical temperature profiles (SHL2, SHL2* and GE3) allow monitoring long-term variations of lake stratification. The correct representation of vertical stratification in the model is essential for reproducing the internal variability. The available profiles were compared with the LR results at the nearest horizontal grid point in the model. Two measures were introduced, the Normalized Root Mean Squared Error ($NRMSE$) and the cross correlation. If we indicate the observed vertical profile at a given time as θ_{obs} (a function of the depth coordinate) and the corresponding profile from the numerical simulation as θ_{mod}, the $NRMSE$ is defined as:

$$NRMSE = \frac{\left\langle (\theta_{obs} - \theta_{mod})^2 \right\rangle^{1/2}}{\max[\theta_{obs}] - \min[\theta_{obs}]}, \qquad (1)$$

where the angle brackets indicate depth averaging, and $\max[\cdot]$ and $\min[\cdot]$ are, respectively, the maximum and minimum of the function between the square brackets. The normalization in the definition of the $NRMSE$ allows a comparison of errors during different seasons: The temperature range during winter is a small fraction of that observed during summer. The correlation coefficient is defined as:

$$\rho[\theta_{obs}, \theta_{mod}] = \frac{\left\langle (\theta_{obs} - <\theta_{obs}>)(\theta_{mod} - <\theta_{mod}>) \right\rangle}{\left\langle (\theta_{obs} - <\theta_{obs}>)^2 \right\rangle^{1/2} \left\langle (\theta_{mod} - <\theta_{mod}>)^2 \right\rangle^{1/2}} \qquad (2)$$

$NRMSE$ values for each of the available profiles are shown in the upper panel of Figure S1 as a function of time. The results for the SHL2* deep profiles, available every 30 s, are subsampled at a daily rate in the plot (the error estimates have small variations in time). The correlation coefficients are given in the lower panel of Figure S1.

GE3 profiles at the beginning of the simulation have much larger $NRMSE$ and lower correlations than the later profiles. This poor initial result for the GE3 profiles is due to the initialization of the LR model with a uniform stratification (measured at SHL2) throughout the basin. The results at GE3 continue improving until approximately March 2014, and stabilize afterwards. It can thus be assumed that the LR model spin up ends by early spring 2014. A trend towards lower $NRMSE$ and higher correlations is observed for the SHL2 profiles during the first months of the simulation. It cannot, however, be distinguished from the seasonal variation observed the following year.

Overall, the results are good in terms of both metrics, with particularly good results obtained during the strongly stratified season (June to September). The least satisfactory results in terms of $NRMSE$ are found during winter in the

deep lake (SHL2*). However, these should not be overemphasized, since stratification is very weak in these profiles (i.e., the denominator of the $NRMSE$ is small) and correlation remains good. The LR model has a systematic cold bias with respect to observations below 50-100 m, in both the SHL2 and SHL2* profiles, in the order of 0.1-0.2° C. The cause of this bias is unclear, and may be due to the constant uniform salinity. The fact that it does not increase during the simulation confirms that model drift is negligible.

The substantially heavier computational burden of the HR simulations do not permit a systematic validation over an extended period of time. Therefore, the HR configuration was tested by initializing it as was done for the LR model, and running it until the end of March 2014. Based on the measures described above, the results of the HR model are as good or better than those of the LR model.

Response to wind forcing at Buchillon

Water velocity measurements are available in Buchillon (Buc) at a depth of 26 m. The long time series of velocity measurements permits systematic investigations of the model performance under different wind conditions. Winds over Lake Geneva were studied by *Lemmin and D'Adamo* [1997] for summertime conditions, and more recently by *Razmi et al.* [2013] focusing on the northern part of the lake. We characterize wind forcing by computing the average wind velocity and direction on a daily basis and over the entire lake. This choice provides a manageable amount of data and emphasizes large-scale forcing. These daily and basin averages of wind speed will hereinafter be referred to as the "mean wind".

The analysis of the mean wind during the entire model simulation confirms that mean winds predominantly come from two directions, the northeast (Bise wind) and the southwest (Vent wind) [*Lemmin and D'Adamo*, 1997]. Typical mean wind speed is in the order of a few meters per second along the dominant directions, and can reach up to $10 \, \mathrm{m \, s^{-1}}$ for Bise wind events.

To compare the model performance under different mean wind conditions, measured current velocities at Buchillon were binned according to the mean wind direction at the measurement time. In each bin, the current velocity distribution is described by computing its mean, as well as the percentiles 0, 10, 50, 90 and 100. The results are summarized in Figure S2 as a function of the mean wind direction (the angle refers to the direction the wind is coming from).

For simplicity, we only consider current velocity magnitude. The current velocity distributions from the field observations (bottom left panel) and from the model (bottom right panel) in Figure S2 are remarkably similar, and have strong positive skewness. Model velocities generally overestimate the observed ones; Section 3.1.1 discusses why we attribute this to limitations in the numerical discretization of real bathymetry. Since winds coming from the southwest have the longest fetch over the lake, they lead to the strongest currents. Bise events produce weaker currents, at least at this location along the northern shore of the lake. In the model, and to a lesser extent in the observations, southeast and northwest winds produce stronger-than-average currents, but these winds rarely occur over the lake.

References

Adcroft, A., C. Hill, and J. Marshall (1997), Representation of topography by shaved cells in a height coordinate ocean model, *Monthly Weather Review*, *125*, 2293–2315, doi: 10.1175/1520-0493(1997)125<2293:ROTBSC>2.0.CO;2.

Bouffard, D., and U. Lemmin (2013), Kelvin waves in Lake Geneva, *Journal of Great Lakes Research*, *39*, 637–645, doi: 10.1016/j.jglr.2013.09.005.

Dorostkar, A., L. Boegman, P. J. Diamessis, and A. Pollard (2010), Sensitivity of MITgcm to different model parameters in application to Cayuga Lake, in *Environmental Hydraulics, Two Volume Set: Proceedings of the 6th International Symposium on Environmental Hydraulics, Athens, Greece, 23-25 June 2010*, p. 373.

Gaspar, P., Y. Grégoris, and J.-M. Lefevre (1990), A simple eddy kinetic energy model for simulations of the oceanic vertical mixing: Tests at station Papa and long-term upper ocean study site, *Journal of Geophysical Research: Oceans*, *95*, 16,179–16,193, doi:10.1029/JC095iC09p16179.

Griffies, S. M., and R. W. Hallberg (2000), Biharmonic friction with a Smagorinsky-like viscosity for use in large-scale eddy-permitting ocean models, *Monthly Weather Review*, *128*, 2935–2946, doi: 10.1175/1520-0493(2000)128<2935:BFWASL>2.0.CO;2.

Hill, C., D. Ferreira, J.-M. Campin, J. Marshall, R. Abernathey, and N. Barrier (2012), Controlling spurious diapycnal mixing in eddy-resolving height-coordinate ocean models – Insights from virtual deliberate tracer release experiments, *Ocean Modelling*, *45-46*, 14–26, doi:10.1016/j.ocemod.2011.12.001.

Large, W. G., and S. G. Yeager (2004), Diurnal to decadal global forcing for ocean and sea-ice models: The data sets and flux climatologies, *Tech. rep.*, National Center for Atmospheric Research, Boulder, USA.

Lemmin, U., and N. D'Adamo (1997), Summertime winds and direct cyclonic circulation: Observations from Lake Geneva, *Annales Geophysicae*, *14*, 1207–1220, doi: 10.1007/s00585-996-1207-z.

Marshall, J., A. Adcroft, C. Hill, L. Perelman, and C. Heisey (1997), A finite-volume, incompressible Navier Stokes model for studies of the ocean on parallel computers, *Journal of Geophysical Research: Oceans*, *102*, 5753–5766, doi: 10.1029/96JC02775.

McDougall, T. J., D. R. Jackett, D. G. Wright, and R. Feistel (2003), Accurate and computationally efficient algorithms for potential temperature and density of seawater, *Journal of Atmospheric and Oceanic Technology*, *20*, 730–741, doi: 10.1175/1520-0426(2003)20<730:AACEAF>2.0.CO;2.

MeteoSwiss, NWP department (2017), Personal communication.

Paulson, C. A., and J. J. Simpson (1977), Irradiance measurements in the upper ocean, *Journal of Physical Oceanography*, *7*, 952–956, doi: 10.1175/1520-0485(1977)007<0952:IMITUO>2.0.CO;2.

Prather, M. J. (1986), Numerical advection by conservation of second-order moments, *Journal of Geophysical Research: Atmospheres*, *91*, 6671–6681, doi:10.1029/JD091iD06p06671.

Razmi, A. M., D. A. Barry, U. Lemmin, F. Bonvin, T. Kohn, and R. Bakhtyar (2013), Direct effects of dominant winds on residence and travel times in the wide and open lacustrine embayment: Vidy Bay (Lake Geneva, Switzerland), *Aquatic Sciences*, *76*, 59–71, doi:10.1007/s00027-013-0321-8.

Wüest, A., and A. Lorke (2003), Small-scale hydrodynamics in lakes, *Annual Review of Fluid Mechanics*, *35*, 373–412, doi: 10.1146/annurev.fluid.35.101101.161220.

Corresponding author: A. Cimatoribus, Ecological Engineering Laboratory (ECOL), Institute of Environmental Engineering, School of Architecture, Civil and Environmental Engineering, École Polytechnique Fédérale de Lausanne (EPFL), 1015 Lausanne, Switzerland. (andrea.cimatoribus@epfl.ch)
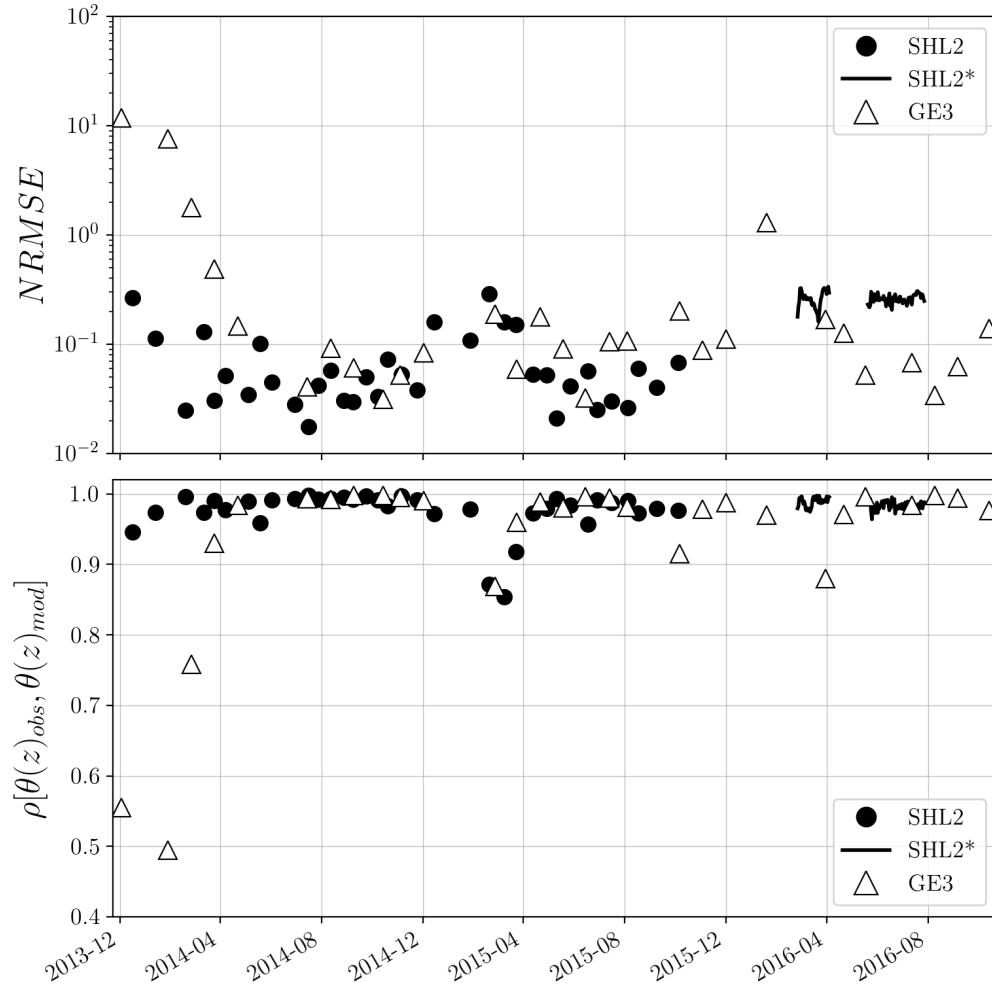
Figure S1. The upper panel shows the $NRMSE$ of temperature profiles in the model with respect to the measured ones (at SHL2, SHL2* and GE3, see legend). Note that the vertical axis is logarithmic. The lower panel presents the correlation coefficient between the numerical and observed profiles. The date of the observation is given on the horizontal axis (year-month).
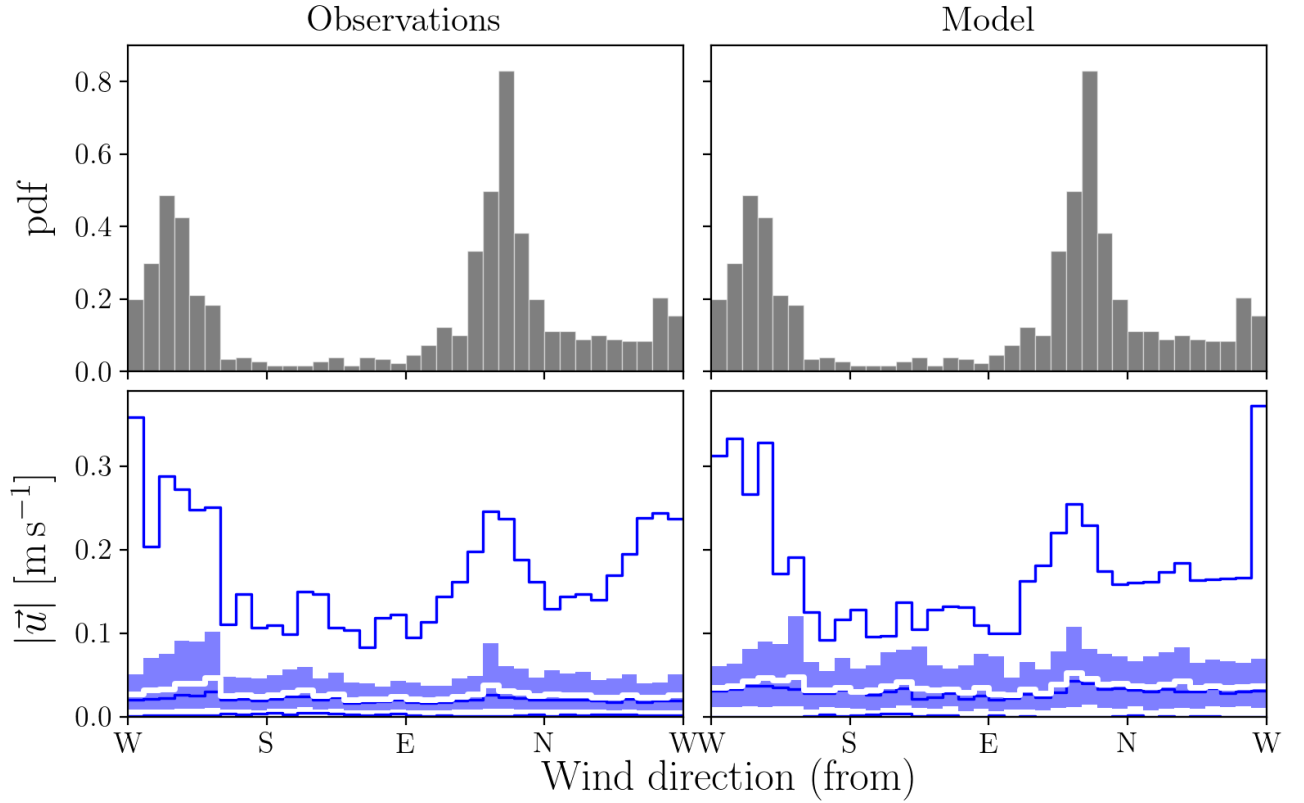
Figure S2. The upper panels are identical and show the probability density function (pdf) of the mean wind direction for the time of the simulation (initial spin up excluded) from 1 January 2014 to 31 October 2016. The direction is the one the wind is coming from, and is labeled West (W), South (S), East (E) or North (N). The lower panels provide a description of the distributions of the vector magnitude of current velocity ($|\vec{u}|$) at the Buchillon field station in each bin (of wind angle) as follows: The lower blue line (barely visible) is the minimum, the mid blue line is the 50th percentile and the upper blue line is the maximum. The shaded part identifies the region between the 10th and 90th percentiles, the core of the distribution. The thick white line is the mean. The lower left panel shows the results from the observations and the lower right panel gives the results from the model.
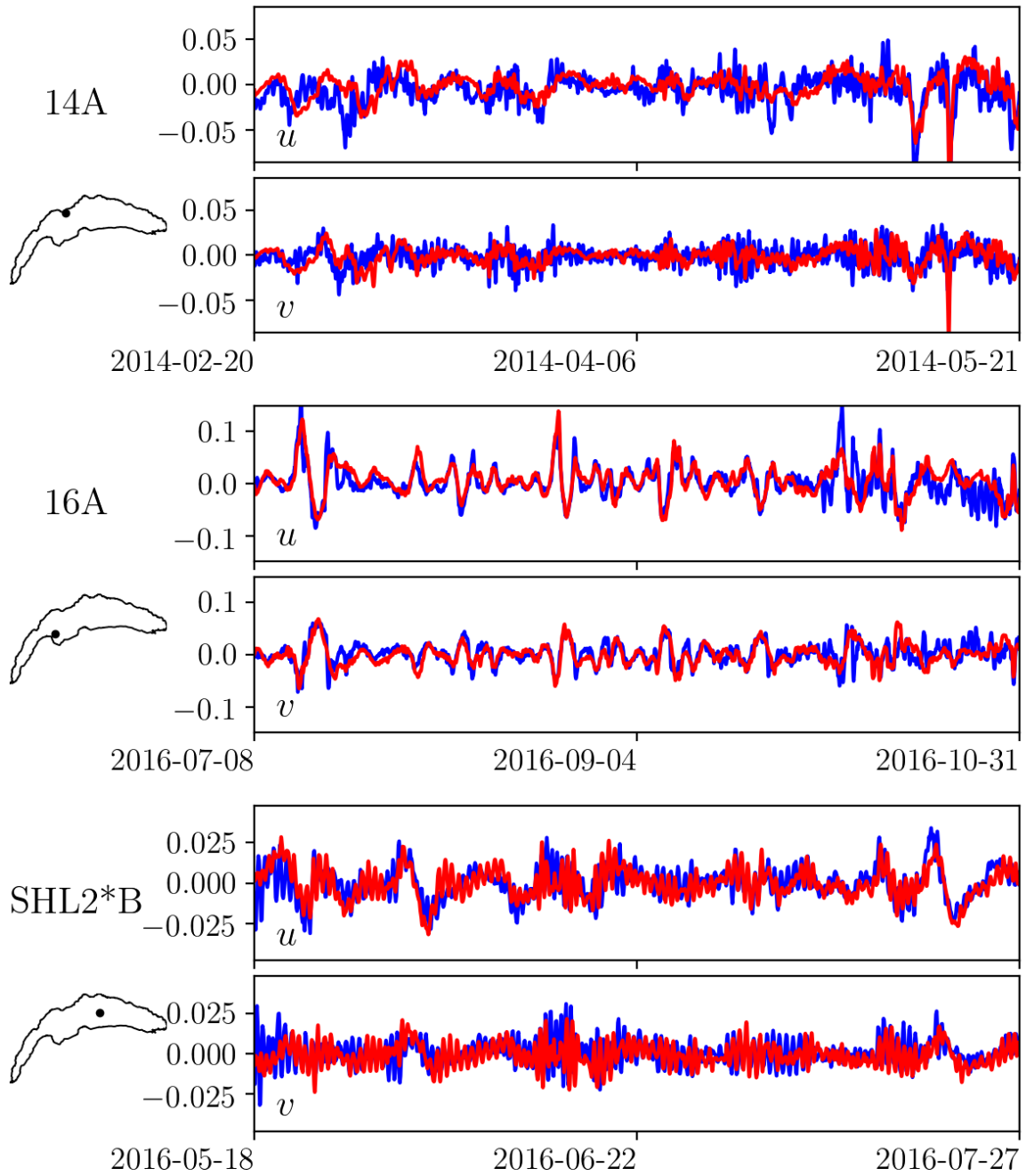
Figure S3. Comparison of velocity time series from the field observations (blue) and from the model (red). Velocity is vertically averaged as discussed in the main text (Section 2.4). Three stations are shown: 14A, 16A and SHL2*B. On the left, a small map indicates the position of the field station in the lake with a black dot (see also Table 1 in the main paper). For each station, the two components are given in units of $m\,s^{-1}$: eastward u in the upper panel, and northward v in the lower panel. The horizontal and vertical scales are different for each station.
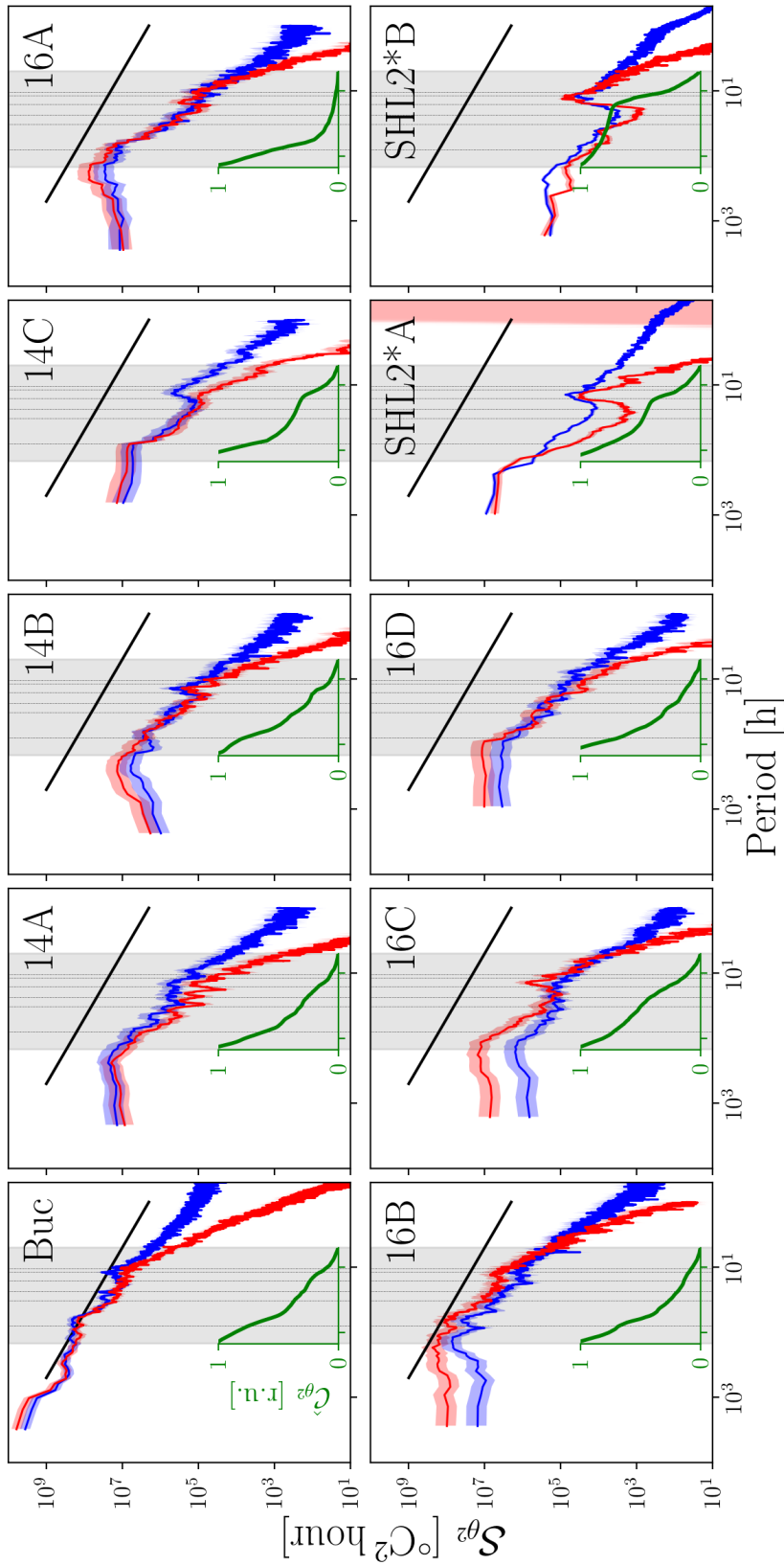
Figure S4. Temperature variance spectra, S_{θ^2}, computed from observational (blue) and model (red) data, with 95% confidence intervals shaded with the corresponding color, as in Figure 3 in the main text. The inset in each panel (green color) shows the temperature variance cumulative spectral distributions, C_{θ^2}, from observations, computed in the shaded range ($1/\nu_0 = 150\,\mathrm{h}$ to $1/\nu_1 = 5\,\mathrm{h}$, see Section 2.4). Note that the inset shares the horizontal axis with the main plot, while it uses relative units in the vertical. Refer to Table 1 and Figure 1 for acronyms and locations. The vertical dashed lines identify some notable periods, from left to right, in hours: 81.5 (Kelvin mode 1), 33.3 (Kelvin mode 3), 24 (diurnal), 16.5 (inertial/Coriolis), 12 (semidiurnal) and 10.6 (Poincaré mode 1). The thick black line is a guide for the eye corresponding to a power-law with $\alpha = -1$.